



i FACULTEIT
INGENIEURSWETENSCHAPPEN

B-KUL-H04X3A: Control Theory

Team 47:

Lefebure Tiebert (r0887630)
Campaert Lukas (r0885501)

Assignment 5: Estimation and control of a two-wheel driven cart

Professor:

Prof. Dr. Ir. Jan Swevers

Academic Year 2025-2026

Declaration of Originality

We hereby declare that this submitted draft is entirely our own, subject to feedback and support given us by the didactic team, and subject to lawful cooperation which was agreed with the same didactic team. Regarding this draft, we also declare that:

1. Note has been taken of the text on academic integrity <https://eng.kuleuven.be/studeren/mastoproef-en-papers/documenten/20161221-academische-integriteit-okt2016.pdf>.
2. No plagiarism has been committed as described on <https://eng.kuleuven.be/studeren/mastoproef-en-papers/plagiaat#Definitie: Wat is plagiaat?>.
3. All experiments, tests, measurements, . . . , have been performed as described in this draft, and no data or measurement results have been manipulated.
4. All sources employed in this draft – including internet sources – have been correctly referenced.

1 Modeling the system

1.1 State equation (1a)

The two-wheel driven (2WD) cart has two independently controlled wheels with angular velocities ω_L (left) and ω_R (right). Let r denote the wheel radius and a denote the half-wheelbase (distance from the cart centre to each wheel). The kinematic relations between wheel speeds and the cart's forward velocity v and rotational velocity ω are given by

$$v = \frac{r}{2}(\omega_L + \omega_R), \quad \omega = \frac{r}{2a}(\omega_R - \omega_L). \quad (1)$$

Inverting these relations yields the required motor commands for a given (v, ω) pair:

$$\omega_L = \frac{1}{r}(v - a\omega), \quad \omega_R = \frac{1}{r}(v + a\omega). \quad (2)$$

With the state vector $\xi = [x_c \ y_c \ \theta]^T$ representing the 2D pose of the cart in the world frame XY , and the input vector $\mathbf{u} = [v \ \omega]^T$, the nonlinear continuous-time state equations are

$$\dot{\xi} = f(\xi, \mathbf{u}) = \begin{bmatrix} v \cos \theta \\ v \sin \theta \\ \omega \end{bmatrix}, \quad \xi(t_0) = [x_0 \ y_0 \ \theta_0]^T. \quad (3)$$

This model assumes ideal velocity control (the velocity control loop is closed internally) and no wheel slip, as specified in the assignment.

1.2 Measurement equation for both IR sensors (1b)

A wall is characterised by the implicit equation $\mathcal{W} = \{(x, y) \mid px + qy = r\}$. The unit normal to the wall is $\hat{\mathbf{n}} = \frac{1}{\sqrt{p^2+q^2}}[p \ q]^T$. The signed perpendicular distance from a point (x, y) to the wall is

$$d(x, y; p, q, r) = \frac{r - px - qy}{\sqrt{p^2 + q^2}}. \quad (4)$$

The cart is equipped with two infrared (IR) sensors: a frontal sensor and a lateral sensor. The geometric offsets of these sensors, measured in the body frame $X'Y'$, are as follows. The front sensor has a longitudinal offset α from the cart centre along the X' -axis, while the side sensor has a longitudinal offset β along X' combined with a lateral offset γ along $-Y'$. For the platform under consideration, these dimensions are $\alpha = 0.075$ m, $\beta = 0.065$ m, and $\gamma = 0.078$ m. The sensor positions in world coordinates are obtained by the standard rotation transformation:

$$x_f = x_c + \alpha \cos \theta, \quad y_f = y_c + \alpha \sin \theta, \quad (5)$$

$$x_s = x_c + \beta \cos \theta - \gamma \sin \theta, \quad y_s = y_c + \beta \sin \theta + \gamma \cos \theta. \quad (6)$$

The general nonlinear measurement model for both sensors is

$$\mathbf{z} = h(\xi) + \mathbf{v}_m = \begin{bmatrix} d(x_f, y_f; p_1, q_1, r_1) \\ d(x_s, y_s; p_2, q_2, r_2) \end{bmatrix} + \mathbf{v}_m, \quad \mathbf{v}_m \sim \mathcal{N}(\mathbf{0}, R), \quad (7)$$

where subscripts 1 and 2 denote the wall parameters for the front and side sensors, respectively.

1.2.1 Specific measurement equations for Figure 1

For the configuration shown in Figure 1, wall 1 (horizontal, bottom) is defined by $y = 0$, corresponding to $(p_1, q_1, r_1) = (0, 1, 0)$. Wall 2 (vertical, left) is defined by $x = 0$, corresponding to $(p_2, q_2, r_2) = (1, 0, 0)$. Substituting into (4):

$$z_1 = d(x_f, y_f; 0, 1, 0) = -y_f = -(y_c + \alpha \sin \theta), \quad (8)$$

$$z_2 = d(x_s, y_s; 1, 0, 0) = -x_s = -(x_c + \beta \cos \theta - \gamma \sin \theta). \quad (9)$$

The negative signs indicate that the cart is located in the third quadrant (negative x and y), with the sensors measuring positive distances to walls at $x = 0$ and $y = 0$.

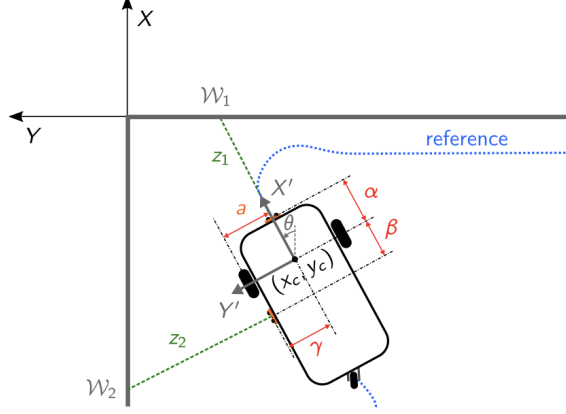


Figure 1: Schematic overview of the robot moving in the world and measuring the distance to the walls. [1]

2 Extended Kalman filter (EKF) derivation and discussion

2.1 Discretization of continuous-time nonlinear model using forward Euler (2a)

The continuous-time state equation (3) is discretised using the forward Euler method with sampling period T_s :

$$\xi_{k+1} = \xi_k + T_s f(\xi_k, \mathbf{u}_k) + \mathbf{w}_k = \begin{bmatrix} x_{c,k} + T_s v_k \cos \theta_k \\ y_{c,k} + T_s v_k \sin \theta_k \\ \theta_k + T_s \omega_k \end{bmatrix} + \mathbf{w}_k, \quad (10)$$

where $\mathbf{w}_k \sim \mathcal{N}(\mathbf{0}, Q)$ represents additive process noise [2].

The measurement equation, being algebraic rather than differential, requires no discretisation:

$$\mathbf{z}_k = h(\xi_k) + \mathbf{v}_k, \quad \mathbf{v}_k \sim \mathcal{N}(\mathbf{0}, R). \quad (11)$$

2.2 Linearization of discrete-time model around state ξ^* (2b)

2.2.1 Choice of linearization point ξ^*

The extended Kalman filter (EKF) linearises the nonlinear model around the current state estimate at each time step. For the prediction step, linearisation is performed around $\xi^* = \hat{\xi}_{k|k}$ (the a posteriori estimate from the previous step). For the correction step, linearisation is performed around $\xi^* = \hat{\xi}_{k|k-1}$ (the a priori prediction).

In contrast, a standard linear Kalman filter (KF) would use a fixed linearisation point, typically chosen as the initial state or a nominal operating point. This distinction is critical: the EKF adapts its linear approximation as the state evolves, whereas the linear KF maintains constant system matrices. For trajectories involving significant heading changes (such as the 90° turn in this assignment), the fixed-linearisation approach introduces substantial model mismatch, degrading filter performance.

2.2.2 State Jacobian

The Jacobian of the discrete-time state equation with respect to ξ is

$$A_k = \frac{\partial}{\partial \xi} [\xi + T_s f(\xi, \mathbf{u})] \Big|_{\xi^*, \mathbf{u}^*} = \begin{bmatrix} 1 & 0 & -T_s v^* \sin \theta^* \\ 0 & 1 & T_s v^* \cos \theta^* \\ 0 & 0 & 1 \end{bmatrix}. \quad (12)$$

The input Jacobian is

$$B_k = \frac{\partial}{\partial \mathbf{u}} [\boldsymbol{\xi} + T_s f(\boldsymbol{\xi}, \mathbf{u})] \Big|_{\boldsymbol{\xi}^*, \mathbf{u}^*} = \begin{bmatrix} T_s \cos \theta^* & 0 \\ T_s \sin \theta^* & 0 \\ 0 & T_s \end{bmatrix}. \quad (13)$$

2.2.3 Measurement Jacobian (general)

For the general measurement equation (7), the Jacobian with respect to $\boldsymbol{\xi}$ is

$$C_k = \begin{bmatrix} -\frac{p_1}{n_1} & -\frac{q_1}{n_1} & -\frac{p_1 \frac{\partial x_f}{\partial \theta} + q_1 \frac{\partial y_f}{\partial \theta}}{n_1} \\ -\frac{p_2}{n_2} & -\frac{q_2}{n_2} & -\frac{p_2 \frac{\partial x_s}{\partial \theta} + q_2 \frac{\partial y_s}{\partial \theta}}{n_2} \end{bmatrix}, \quad (14)$$

where $n_i = \sqrt{p_i^2 + q_i^2}$ and the partial derivatives are

$$\frac{\partial x_f}{\partial \theta} = -\alpha \sin \theta^*, \quad \frac{\partial y_f}{\partial \theta} = \alpha \cos \theta^*, \quad (15)$$

$$\frac{\partial x_s}{\partial \theta} = -\beta \sin \theta^* - \gamma \cos \theta^*, \quad \frac{\partial y_s}{\partial \theta} = \beta \cos \theta^* - \gamma \sin \theta^*. \quad (16)$$

2.2.4 Measurement Jacobian for Figure 1

Substituting $(p_1, q_1) = (0, 1)$ and $(p_2, q_2) = (1, 0)$ into (14) yields

$$C_k = \begin{bmatrix} 0 & -1 & -\alpha \cos \theta^* \\ -1 & 0 & \beta \sin \theta^* + \gamma \cos \theta^* \end{bmatrix}. \quad (17)$$

The linearised discrete-time model is thus

$$\delta \boldsymbol{\xi}_{k+1} = A_k \delta \boldsymbol{\xi}_k + B_k \delta \mathbf{u}_k + \mathbf{w}_k, \quad (18)$$

$$\delta \mathbf{z}_k = C_k \delta \boldsymbol{\xi}_k + \mathbf{v}_k. \quad (19)$$

2.3 Linear vs. extended Kalman filter (2c)

2.3.1 Fundamental differences

The **linear Kalman filter** assumes that both the process model and measurement model are linear (or have been linearised about a fixed operating point). All prediction and correction steps use constant matrices A , B , and C . This approach is optimal (in the minimum mean-squared error sense) when the underlying system is truly linear and the noise distributions are Gaussian.

The **extended Kalman filter** applies to nonlinear systems by linearising the process and measurement models at each time step around the current state estimate. The Jacobians A_k , B_k , and C_k are recomputed at every iteration. The prediction step uses the full nonlinear model $f(\cdot)$ to propagate the state estimate, while the covariance propagation uses the linearised Jacobian A_k .

2.3.2 Noise considerations

Both filters assume the same stochastic structure: additive Gaussian process noise with covariance Q and additive Gaussian measurement noise with covariance R . There is no inherent reason for these covariances to differ between filter types; they characterise the physical system and sensors, not the estimation algorithm.

2.3.3 Applicability

The linear KF is appropriate when the system dynamics are linear or when the state remains sufficiently close to the linearisation point that model mismatch is negligible. For the 2WD cart executing a 90° turn, the heading θ changes substantially, causing the trigonometric terms in the state and measurement equations to vary significantly. A fixed-linearisation linear KF would exhibit increasing estimation error as θ deviates from the nominal value. The EKF, by continuously updating its linearisation point, maintains local accuracy throughout the trajectory and is therefore the appropriate choice for this application.

3 Extended Kalman filter design and implementation

3.1 Noise sources: measurement noise and process noise (3a)

The process noise covariance Q accounts for discrepancies between the assumed kinematic model and the actual cart dynamics. Wheel slip constitutes a primary source, as the no-slip assumption is violated under acceleration, deceleration, or on low-friction surfaces. Velocity command tracking error also contributes, since the internal velocity control loop does not achieve perfect tracking and transient errors between commanded and realised wheel speeds propagate to pose estimation. Furthermore, the passive swivel wheel introduces unmodelled lateral forces and yaw disturbances, particularly during turns. Finally, geometric uncertainties arising from imprecise knowledge of wheel radius r and wheelbase $2a$ cause systematic drift that manifests as process noise.

The measurement noise covariance R accounts for uncertainty in the IR range measurements. Electronic noise in the IR sensor circuitry and quantisation in the ADC represent inherent sensor noise. Wall reflectivity variation poses an additional challenge, as IR sensors are sensitive to surface properties and non-uniform reflectivity causes range-dependent bias. Sensor mounting uncertainty, specifically errors in the measured offsets α , β , and γ , directly biases the measurement equations. At oblique incidence angles, multipath and specular reflections can also cause erroneous range readings.

3.2 Extended Kalman filter design and tuning (3b)

3.2.1 Interpretation of Q and R

The process noise covariance $Q = \text{diag}(q_x, q_y, q_\theta)$ quantifies the expected variance of the state perturbation per time step. Larger values of Q indicate lower confidence in the model prediction, causing the filter to weight measurements more heavily. The measurement noise covariance $R = \text{diag}(r_1, r_2)$ quantifies the expected variance of the sensor readings. Larger values of R indicate lower confidence in the measurements, causing the filter to rely more on the model prediction.

The ratio Q/R governs the filter bandwidth: a high ratio yields fast convergence to measurements but amplifies sensor noise; a low ratio yields smooth estimates but slow response to actual state changes.

3.2.2 Initial state estimate covariance $\hat{P}_{0|0}$

The cart is initialised at the prescribed starting pose:

$$\hat{\xi}_{0|0} = [-0.30 \ -0.20 \ 0]^T \ [\text{m}, \text{m}, \text{rad}]. \quad (20)$$

The initial covariance $\hat{P}_{0|0}$ reflects the placement uncertainty:

$$\hat{P}_{0|0} = \text{diag}(1 \times 10^{-3}, 1 \times 10^{-3}, 7.6 \times 10^{-3}) \ [\text{m}^2, \text{m}^2, \text{rad}^2]. \quad (21)$$

These values reflect realistic placement uncertainty when positioning the cart manually: the translational entries correspond to a standard deviation of approximately 3.2 cm, while the yaw entry corresponds to a standard deviation of approximately 5° . This choice ensures the filter quickly trusts the IR measurements during the initial measurement phase while still allowing for significant initial state mismatch.

3.2.3 Tuned covariance values

Systematic tuning was performed by varying the diagonal entries of Q and R while monitoring the state estimate trajectories and 95% confidence intervals. The selected values are

$$Q = \text{diag}(8 \times 10^{-9}, 9 \times 10^{-8}, 9 \times 10^{-7}) [\text{m}^2, \text{m}^2, \text{rad}^2], \quad (22)$$

$$R = \text{diag}(0.0198, 0.09) [\text{m}^2]. \quad (23)$$

The relatively large R values reflect the non-Gaussian characteristics of the IR sensors at oblique incidence and when only one wall is visible. The small Q values were chosen to maintain bounded dead-reckoning drift during the sensor blackout phase while ensuring the filter remains responsive to measurements during the observation phases.

3.2.4 Q/R sweep results

Four experimental runs were performed with distinct covariance combinations to characterise the sensitivity of the EKF to the Q/R ratio. These configurations comprise the baseline (Q, R) as specified in (22)–(23), a high process noise case ($5Q, R$), a high measurement noise case ($Q, 5R$), and a configuration with both increased ($5Q, 5R$). The resulting state estimates over time for each combination are shown in Figures 2a–2c.

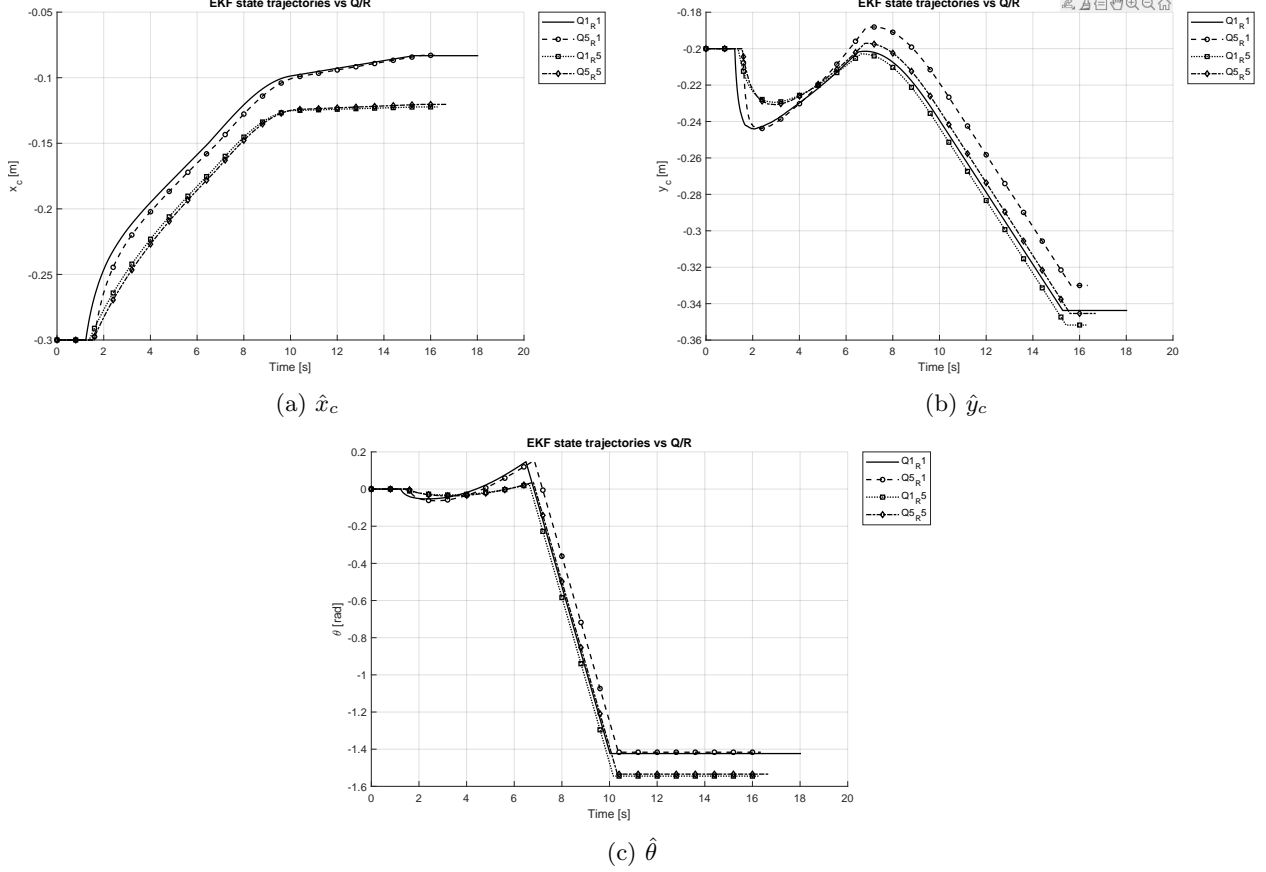


Figure 2: State estimates over time for four (Q, R) combinations: (a) x -position, (b) y -position, (c) heading.

3.2.5 Influence of Q and R on EKF behaviour

The experimental results confirm the expected trade-offs. Increasing Q causes the filter to trust the model less and respond more aggressively to measurements; post-turn convergence is faster when sensors resume, but the estimate exhibits greater noise sensitivity during the straight-line phases. Conversely, increasing R

causes the filter to trust measurements less, yielding smoother estimates at the cost of slower correction after the turn and accumulated lateral bias during the sensor blackout. The baseline (Q, R) configuration provides the optimal balance between responsiveness and smoothness, with estimates converging within acceptable bounds after the turn while maintaining stability during the straight-line phases.

3.3 Uncertainty on the estimated states (3c)

Figures 3a–3c show the state estimates with 95% confidence intervals for the baseline tuned run.

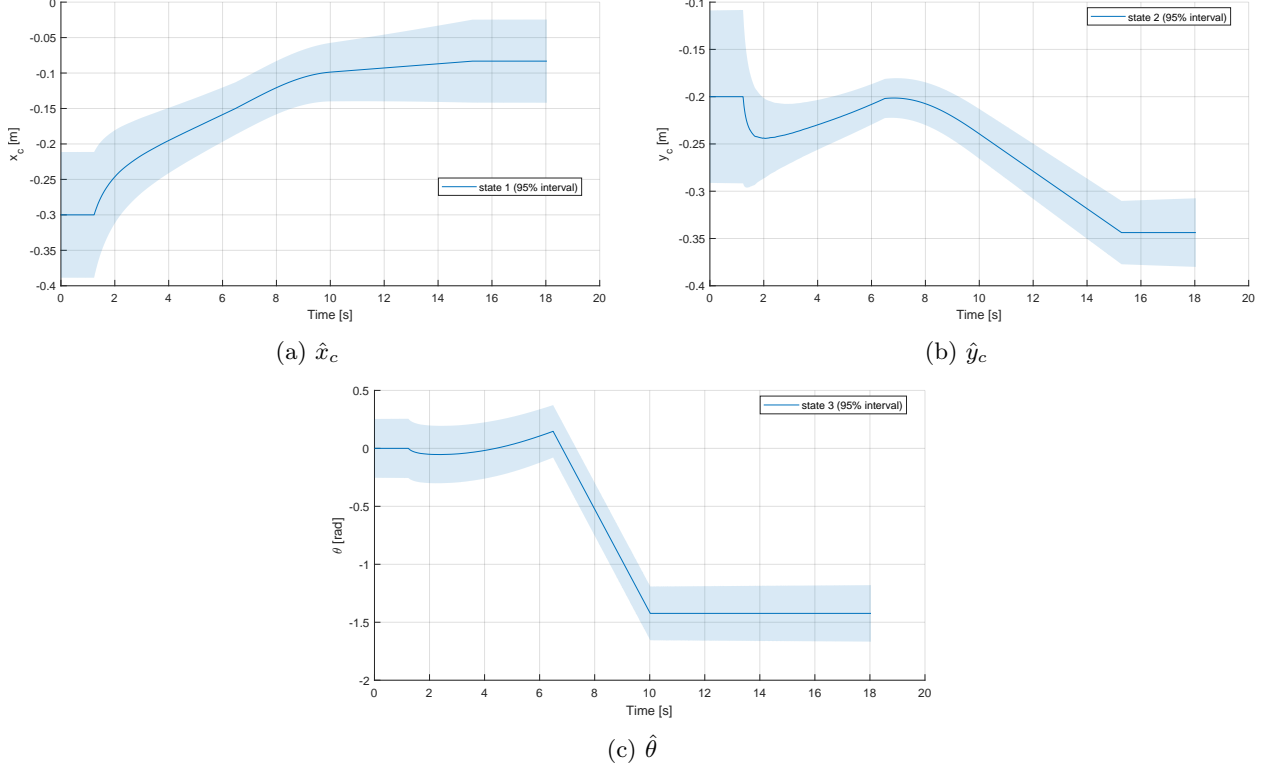


Figure 3: State estimates with 95% confidence intervals for the baseline (Q, R) tuning: (a) x -position, (b) y -position, (c) heading.

3.3.1 Uncertainty evolution by trajectory phase

The uncertainty evolution exhibits distinct behaviour across the three trajectory phases. Before the turn, when both sensors are active, the measurement matrix C_k has rank 2 (full row rank), providing observability for all three states; consequently, the covariance P decreases rapidly as measurements correct the prediction and the confidence intervals tighten. During the turn, with both sensors switched off, the correction step provides no information and only the prediction step is active, causing P to grow according to $P_{k+1|k} = A_k P_{k|k} A_k^T + Q$ and the confidence intervals to widen monotonically. After the turn, only the front sensor measurement z_1 is available; the measurement matrix reduces to rank 1, providing direct observability only for the y -coordinate. Observability of x and θ depends on the coupling through the motion model, resulting in slow decrease of the yaw variance and elevated x -variance due to reduced direct observation.

3.3.2 Effect of sensor deactivation on measurement equations

When both sensors are switched off, the measurement update is skipped entirely. The filter operates in pure prediction mode (dead reckoning), and the state estimate evolves according to the process model without correction.

3.3.3 Hypothetical: sensors remain active during turn

If the sensors were not deactivated during the turn, the measurement equations would change in a non-trivial manner. The front sensor would transition from measuring the distance to wall 1 ($y = 0$) to measuring the distance to wall 2 ($x = 0$) as the cart rotates, and the side sensor would similarly change the wall it observes. Consequently, the wall parameters (p_i, q_i, r_i) in the measurement model would need to be updated dynamically based on the cart's orientation and position, requiring prior knowledge of the environment geometry. While this approach would maintain observability throughout the turn, it necessitates additional logic to determine which wall each sensor is measuring at any given time.

3.3.4 Measurement Predictions and Confidence Intervals

Figures 4a and 4b show the measurement predictions with 95% confidence intervals for the baseline tuned run.

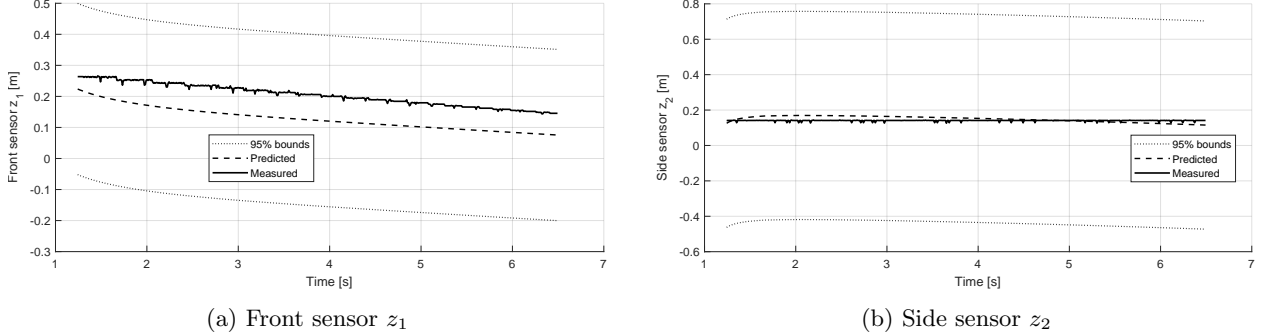


Figure 4: Measurement predictions with 95% confidence intervals for the baseline (Q, R) tuning: (a) front sensor, (b) side sensor.

The 95% bands reflect the tuned R values. The bands widen during the turn when measurements are disabled and the filter relies solely on prediction. After the turn, only z_1 contributes to the correction, leaving residual uncertainty in states not directly observed by the front sensor.

4 State feedback controller design and implementation

4.1 Rotation matrix for error transformation (4a)

The tracking error in the world frame is $\hat{\mathbf{e}}_k = [x_{c,\text{ref}} - \hat{x}_c, y_{c,\text{ref}} - \hat{y}_c, \theta_{\text{ref}} - \hat{\theta}]^T$. To express this error in the local cart frame $X'Y'$, the rotation matrix

$$R(\hat{\theta}_{c,k}) = \begin{bmatrix} \cos \hat{\theta}_{c,k} & \sin \hat{\theta}_{c,k} & 0 \\ -\sin \hat{\theta}_{c,k} & \cos \hat{\theta}_{c,k} & 0 \\ 0 & 0 & 1 \end{bmatrix} \quad (24)$$

is applied: $\hat{\mathbf{e}}'_k = R(\hat{\theta}_{c,k})\hat{\mathbf{e}}_k$.

4.2 LQR feedback matrix structure (4b)

The discrete-time LQR problem minimises the cost function

$$J = \sum_{k=0}^{\infty} (\mathbf{e}'_k^T Q_{\text{lqr}} \mathbf{e}'_k + \mathbf{u}_k^T R_{\text{lqr}} \mathbf{u}_k), \quad (25)$$

where $Q_{\text{lqr}} \in \mathbb{R}^{3 \times 3}$ penalises state error and $R_{\text{lqr}} \in \mathbb{R}^{2 \times 2}$ penalises control effort.

Using the provided linearised error dynamics matrices

$$A_d = \begin{bmatrix} 1 & 0 & 0 \\ 0 & 1 & -T_s v_{\text{ref}} \\ 0 & 0 & 1 \end{bmatrix}, \quad B_d = \begin{bmatrix} -T_s & 0 \\ 0 & 0 \\ 0 & -T_s \end{bmatrix}, \quad (26)$$

the MATLAB `d1qqr` command computes the optimal feedback gain K . The structure of $K \in \mathbb{R}^{2 \times 3}$ is

$$K = \begin{bmatrix} k_{11} & 0 & 0 \\ 0 & k_{22} & k_{23} \end{bmatrix}. \quad (27)$$

The zero entries arise from the decoupled structure of B_d : the forward velocity v affects only the longitudinal error e'_x , while the rotational velocity ω affects the lateral error e'_y (through θ) and the heading error e'_θ . The nonzero entry k_{11} represents the gain from longitudinal error to the forward velocity command, k_{22} represents the gain from lateral error to the rotational velocity command, and k_{23} represents the gain from heading error to the rotational velocity command.

4.3 Systematic approach for LQR tuning (4c)

4.3.1 Meaning of Q_{lqr} and R_{lqr}

In the LQR design objective (25), the weighting matrix Q_{lqr} penalises deviation from the reference trajectory, with larger diagonal entries resulting in tighter tracking of the corresponding state at the expense of higher control effort. Conversely, R_{lqr} penalises control effort, and larger diagonal entries yield smoother, smaller control inputs at the expense of slower convergence. The trade-off is analogous to the Q/R ratio in the EKF: a high $Q_{\text{lqr}}/R_{\text{lqr}}$ ratio yields aggressive tracking with large control signals, while a low ratio yields conservative control with larger tracking errors.

4.3.2 Experimental Results

Four LQR tuning configurations were tested experimentally, differing in their $Q_{\text{lqr}}/R_{\text{lqr}}$ ratios:

- **LQR-A** (baseline): $Q_{\text{lqr}} = \text{diag}(16, 16, 4)$, $R_{\text{lqr}} = \text{diag}(0.1, 0.1)$
- **LQR-B** (doubled state penalty): $Q_{\text{lqr}} = \text{diag}(32, 32, 8)$, $R_{\text{lqr}} = \text{diag}(0.1, 0.1)$
- **LQR-C** (doubled input penalty): $Q_{\text{lqr}} = \text{diag}(16, 16, 4)$, $R_{\text{lqr}} = \text{diag}(0.2, 0.2)$
- **LQR-D** (aggressive): $Q_{\text{lqr}} = \text{diag}(64, 64, 16)$, $R_{\text{lqr}} = \text{diag}(0.05, 0.05)$

No feedforward signals were applied; the closed-loop system relied exclusively on state feedback. The resulting tracking errors in the world frame and body frame are shown in Figure 5, and the corresponding control signals are shown in Figure 6.

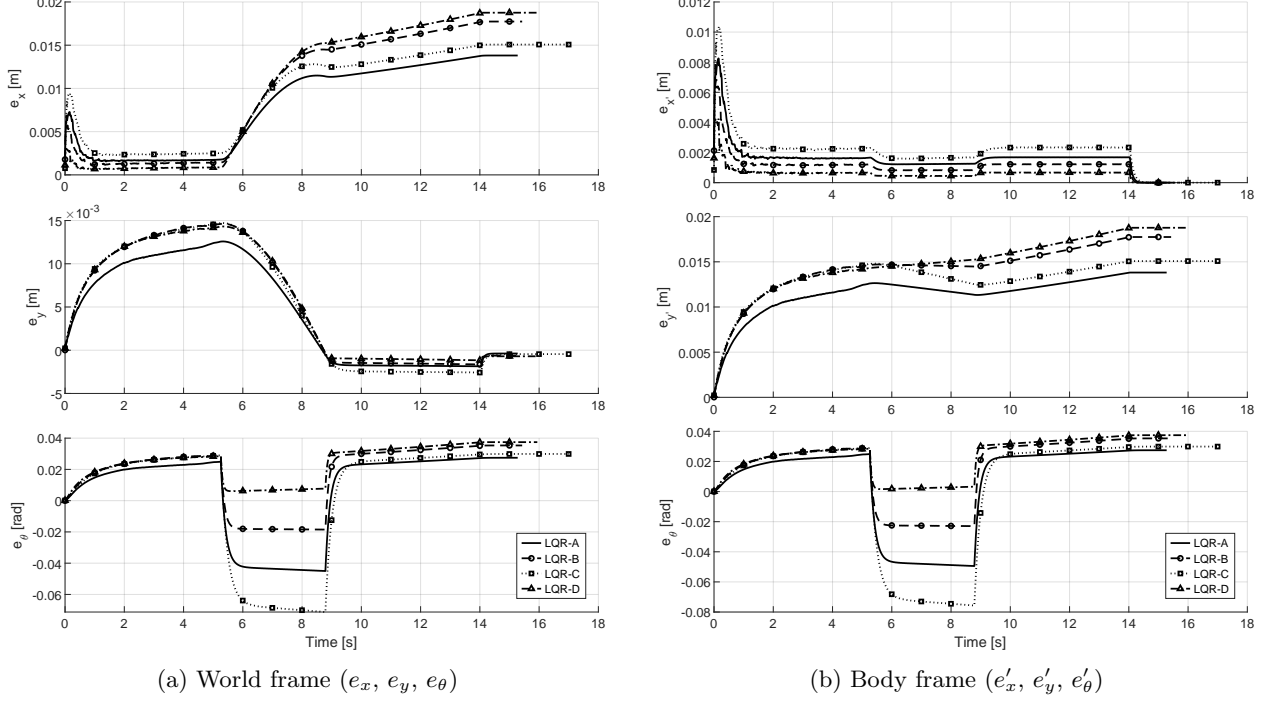


Figure 5: Tracking errors for four LQR tuning configurations. The trajectory comprises a straight segment ($t < 5$ s), a 90° turn ($5 < t < 9$ s), and a final straight segment.

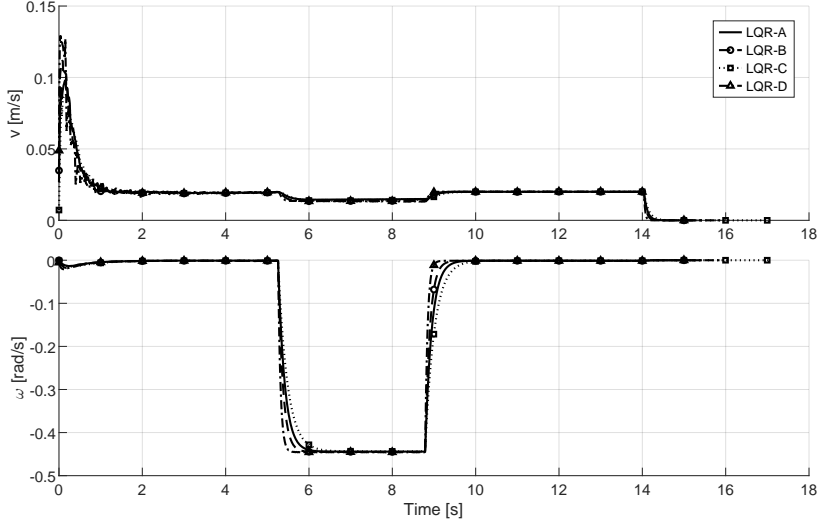


Figure 6: Control signals v and ω for the four LQR configurations.

4.3.3 Effect of different choices of Q_{lqr} and R_{lqr}

The experimental results reveal the characteristic trade-offs in LQR tuning:

- **Convergence speed:** Higher Q_{lqr}/R_{lqr} ratios (LQR-B, LQR-D) yield faster initial convergence. During the startup transient ($t < 1$ s), LQR-D reduces the longitudinal error e'_x most rapidly. However, this aggressive tuning also amplifies the response to measurement noise, visible as increased high-frequency content in the control signals and slight oscillations in the heading error e_θ .

- **Steady-state tracking:** All configurations converge to comparable steady-state errors during the straight-line phases, indicating that the integrator-free LQR does not eliminate static offsets. The residual $e_x \approx 1.5\text{--}2 \text{ cm}$ and $e_\theta \approx 0.02\text{--}0.04 \text{ rad}$ observed after $t = 14 \text{ s}$ reflect unmodelled disturbances (swivel wheel friction, wheel slip) rather than tuning deficiencies.
- **Turn behaviour:** During the 90° turn ($5 < t < 9 \text{ s}$), all controllers exhibit a characteristic dip in e_θ as the heading lags behind the reference. LQR-D recovers most rapidly post-turn, while LQR-C (conservative tuning) shows the slowest recovery. The lateral error e'_y increases substantially during the turn due to the nonlinear coupling between heading and lateral position; the linearised error model (26) captures this coupling only to first order.
- **Control effort:** Figure 6 shows that aggressive tunings (LQR-D) demand larger rotational velocity commands ω during transients. The peak $|\omega|$ during the turn is comparable across configurations, as the reference trajectory itself prescribes a constant $\omega_{\text{ref}} = 0.44 \text{ rad/s}$. The forward velocity v is dominated by the 2 cm/s reference; feedback corrections are small relative to this baseline.
- **Limitations:** Excessively high $Q_{\text{lqr}}/R_{\text{lqr}}$ ratios risk actuator saturation and excitation of unmodelled dynamics (e.g., wheel slip at high ω). Additionally, the LQR design assumes perfect state knowledge; in practice, the EKF estimate $\hat{\xi}$ is used, introducing additional uncertainty that aggressive tunings may amplify.

4.3.4 Chosen values for Q_{lqr} and R_{lqr}

Based on the experimental evaluation, the selected tuning is **LQR-D**:

$$Q_{\text{lqr}} = \text{diag}(64, 64, 16) [\text{m}^{-2}, \text{m}^{-2}, \text{rad}^{-2}], \quad (28)$$

$$R_{\text{lqr}} = \text{diag}(0.05, 0.05) [\text{s}^2/\text{m}^2, \text{s}^2/\text{rad}^2]. \quad (29)$$

This configuration provides the fastest convergence to the reference trajectory while maintaining acceptable control signal magnitudes. The MATLAB `dlqr` command yields the feedback gain matrix

$$K = \begin{bmatrix} 29.95 & 0 & 0 \\ 0 & -32.71 & 16.40 \end{bmatrix}, \quad (30)$$

where the control law is $\mathbf{u} = -K\hat{\xi}'$. The structure confirms the decoupling discussed in Section 4b: the forward velocity correction depends only on the longitudinal error e'_x , while the rotational velocity correction depends on both the lateral error e'_y and the heading error e'_θ . The gain $k_{11} = 29.95$ ensures rapid longitudinal error rejection. The opposite signs $k_{22} < 0$ and $k_{23} > 0$ arise because positive lateral error e'_y requires negative ω correction (turn left), whereas positive heading error e'_θ requires positive ω correction (turn right to catch up).

The units of Q_{lqr} are chosen such that the cost function (25) is dimensionally consistent: since the state errors have units [$\text{m}, \text{m}, \text{rad}$] and the inputs have units [$\text{m/s}, \text{rad/s}$], the diagonal entries of Q_{lqr} carry inverse squared units of the respective states, and those of R_{lqr} carry squared time per squared input units. In practice, one tunes the dimensionless ratios $Q_{\text{lqr},ii}/R_{\text{lqr},jj}$ to achieve the desired transient behaviour.

References

- [1] Jan Swevers. *Control Theory - Assignments*. KU Leuven, 2025.
- [2] Jan Swevers and Goedele Pipeleers. *C10. Optimal Control and Optimal Estimation*. KU Leuven, 2020.